The sequence and structural integrity of the SARS-CoV-2 Spike protein transmembrane domain is crucial for viral entry

Ortiz-Mateu J[1], Belda D[1], Avilés-Alía AI[2], Alonso-Romero J[1], García-Murria MJ[1], Mingarro I[1], Geller R[2], Martinez-Gil L[1*].

[1]Departament de Bioquímica i Biologia Molecular, Institut Universitari de Biotecnologia i Biomedicina (BIOTECMED), Universitat de València, Burjassot, Spain.

[2] Institute for Integrative Systems Biology (I2SysBio), UV-CSIC, Paterna, Spain.

* Corresponding author

Abstract

The Spike protein of SARS-CoV-2 is a type I membrane protein that mediates target cell recognition and membrane fusion. Its transmembrane domain (TMD) is usually considered a passive physical anchor that attaches the protein to the viral envelope. However, current knowledge of the dynamics and biogenesis of integral membrane proteins indicates that TMDs generally play key functions beyond membrane anchoring. Here, we explored the role of the SARS-CoV-2 Spike protein TMD during viral entry. To do so, we generated a series of amino acid substitutions and insertions within the hydrophobic core of the TMD and analyzed their impact on protein function. Our results indicate that the SARS-CoV-2 Spike protein is highly susceptible to changes in its TMD. Furthermore, the TMD sequence and structural parameters relevant for viral entry are distributed across the entire segment, albeit with a stronger implication of the N-terminal portion. The relative orientation of the regions before and after the TMD was also found to be relevant for particle entry. Finally, our results suggest that the SARS-CoV-2 Spike protein TMD can form homo-oligomers through a motif in which small residues are necessary.

Introduction

It is becoming increasingly clear that a deep understanding of the molecular mechanisms occurring during viral infection is required for an effective rational design of antiviral agents and vaccine immunogens. In the case of SARS-CoV-2, special attention has been given to the entry process and the role that the Spike (S) protein plays in it[1]. The SARS-CoV-2 S protein is a trimeric class I fusion glycoprotein that mediates target cell recognition and membrane fusion[2,3,4]. During post-translational maturation, the full-length protein is cleaved into two subunits, S1 and S2. S1 contains the receptor-binding domain (RBD) and facilitates attachment to the angiotensin-converting enzyme 2 (ACE2) on the host cell surface. S2 drives the fusion of the viral and host membranes and encompasses the fusion peptide, two heptad repeat regions, and a C-terminal transmembrane domain (TMD).

Often, the TMD is seen as a passive physical anchor whose sole function is to attach the protein to the viral envelope. However, current knowledge of the structure, dynamics, and biogenesis of integral membrane proteins demonstrates that TMDs, alongside membrane-proximal regions, play key functions beyond membrane anchoring[5–7]. Furthermore, in recent years, significant advances in understanding the role of the TMDs of viral fusion proteins have been made highlighting their critical role in the fusion process, and also demonstrating their involvement in several aspects of the viral lifecycle[8,9].

Broer et al. demonstrated that substituting the N-terminal membrane proximal region, the TMD, and the endodomain of the SARS-CoV-1 S protein with the corresponding domains of the vesicular stomatitis virus (VSV) Glycoprotein greatly affect the protein's function[10]. A few years later, a mutagenesis-based study, once again using VSV pseudo-particles, revealed that substituting Gly_{1201}, Ala_{1204}, Val_{1210}, and Leu_{1216} by Lys residues in the core hydrophobic region of the SARS-CoV-1 S protein resulted in reduced infectivity[11] likely by altering the hydrophobic nature of the TMD.

The SARS-CoV-2 S protein TMD has been linked with trimerization. A chimera including the RBD followed by the TMD was identified as a trimer in which the RBD was properly folded, suggesting that the TMD acts as an oligomerization domain[12]. However, there is some controversy regarding the oligomerization motif within the TMD. Abery et al. identified a GxxxG motif (a sequence known to promote oligomerization of TMDs[13]) within the TMD of the SARS-CoV-1 S protein and demonstrated its importance in the trimerization of the protein[14]. Shortly after, Corver et al.'s results indicated that these residues were not important for the trimerization of the protein or viral entry[15]. Recently, it has been suggested that a new motif based on a hydrophobic zipper mediates the trimerization of SARS-CoV-2 S protein TMD[16].

Several structures of the S protein have been solved. However, only one includes the TMD[17]. In this structure, the S protein was found in a post-fusion state where the fusion peptide (FP) forms a hairpin-like wedge spanning the entire lipid bilayer and the TMD wraps around it. Two contact points between the FP and the TMD were described involving Phe_{1220} and Leu_{1234} on the TMD.

Here, we explore the role of the SARS-CoV-2 S protein TMD during viral entry. To do so we generate a series of variations within the hydrophobic core of the TMD and analyze their impact on the protein function. Furthermore, we investigate the potential of the TMD to induce oligomerization as well as the structural and sequence parameters responsible for it. Our results demonstrate that the SARS-CoV-2 S protein TMD plays a key role in the protein function beyond membrane anchoring. The sequence and structural parameters of the TMD relevant for viral entry are distributed across the entire segment, which might explain its strong sequence conservation and the literature controversy. Additionally, our results suggest that the relative orientation of the regions before and after the TMD is important for particle entry. Finally, we identify that the SARS-CoV-2 S protein TMD is capable

of forming homo-oligomers and these occur through a motif in which small residues such as glycine and alanine are relevant, results that were corroborated *in silico*.

Results

Pseudotyped-VSV particles for the analysis of viral entry

The SARS-CoV-2 S protein contains a single TMD in the C-terminal region of the protein (Fig. 1A). It spans 23 amino acids from Trp_{1214} to Cys_{1236} with a predicted ΔG_{app} of -3,4 kcal/mol for its insertion into the membrane, according to the *ΔG Prediction Server*[18,19]. The predicted TMD includes an aromatic-rich region (Trp_{1214}-Tyr-Ile-Trp_{1217}) in its N-terminal end and a Cys pair (Cys_{1235}-Cys_{1236}) in its C-terminal end. However, the structure of the S trimer in its post-fusion state[17] shows a helical secondary structure from Leu_{1218} to Leu_{1234}. Although the aromatic region and the C-terminal Cys-rich section on the TMD most likely interact with the membrane either as an interfacial membrane proximal region[17,20] or through palmitoyl post-translational modifications[21–24], in the present study we focus exclusively on the helical hydrophobic core of the TMD, that is, from Leu_{1218} to Leu_{1234}. The sequence of all the variants and mutations included in this paper and their insertion potential can be found in Fig.1B. Fig 1C includes a structural model and a helical wheel projection of the SARS-CoV-2 S protein TMD hydrophobic core.

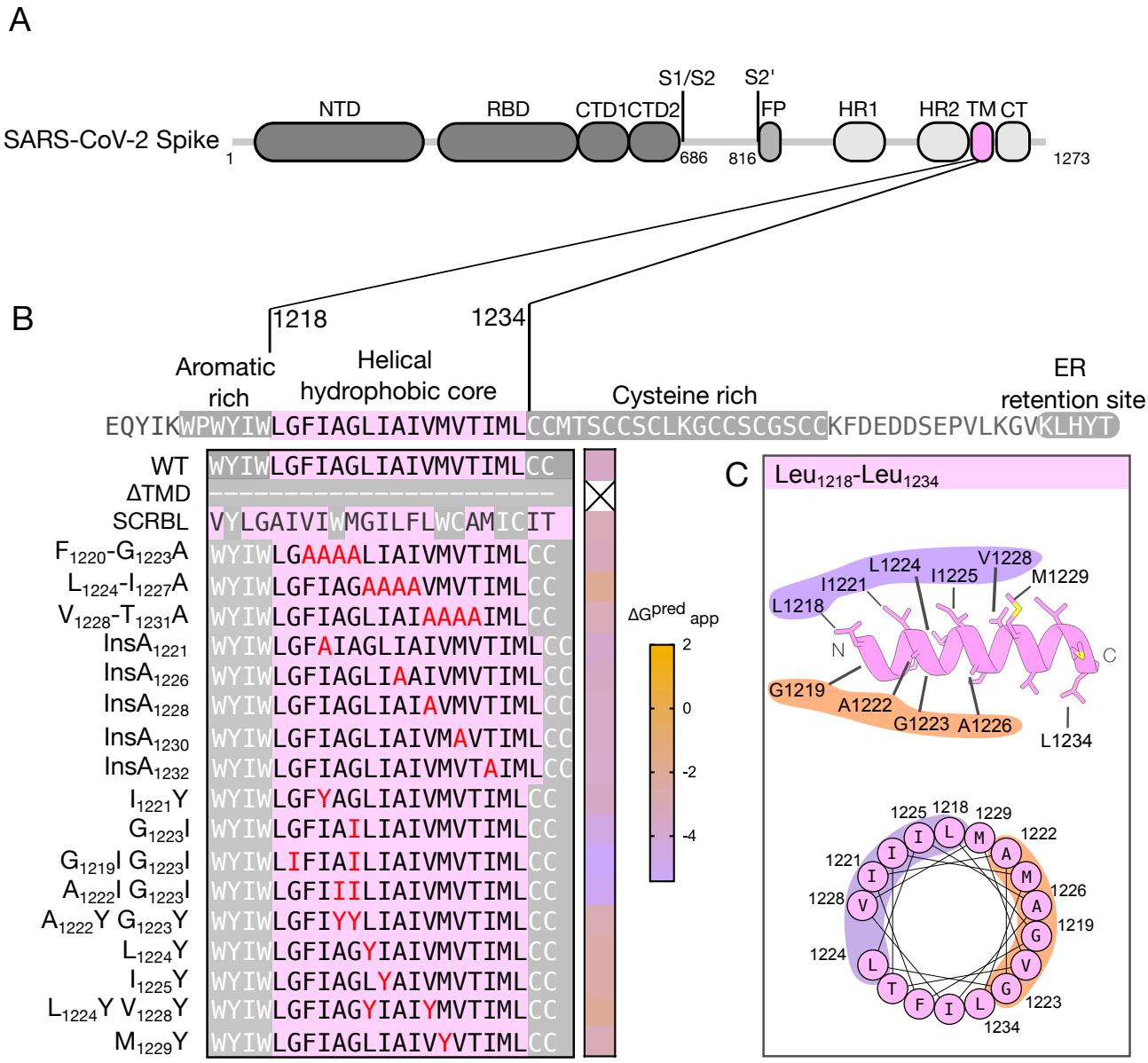

Figure 1. Schematic representation of the SARS-CoV-2 spike protein and its TMD. **A**. Schematic representation of SARS-CoV-2 Spike protein domain architecture. The position of key domains is highlighted: NTD, N-terminal domain; RBD, Receptor Binding Domain; CTD1, C-terminal domain 1; CTD2, C-terminal domain 2; S1/S2, S1/S2 cleavage site; S2′, S2′ cleavage site; FP, fusion peptide; HR1, heptad repeat 1; HR2, heptad repeat 2; TM, transmembrane domain; CT, cytoplasmic tail. **B**. Sequence of the SARS-CoV-2 S protein TMD and the variants included in this study. The sequence of the SARS-CoV-2 S protein from Glu_{1206} to Thr_{1273} is shown. Membrane-associated regions, including an aromatic-rich section and a cysteine-rich domain, are highlighted with light letters on a gray background. The TMD hydrophobic core is shown with dark letters on a pink background. The TMD, as predicted by the ΔG Prediction Server (WT), and the variations included in this work are highlighted. A heat map (right of the sequence) shows the predicted ΔG_{app} for each TMD variant. **C**. Structural model of the SARS-CoV-2 S protein TMD. AlphaFold3 model of residues 1218-1234 (top)

103 and helical wheel projection (bottom) of the same sequence. The surface of the helix containing small side chain residues
104 is highlighted in orange, while the opposite surface containing highly hydrophobic residues is highlighted in purple.
105
106 To study the role of the SARS-CoV-2 S protein TMD during viral entry we utilized pseudotyped
107 vesicular stomatitis virus (VSV) particles coated with different S protein variants (Fig. 2A)[10,15,25,26].
108 Briefly, HEK293T cells were transfected with plasmids encoding the different S variants and
109 subsequently infected with a recombinant VSV in which the glycoprotein gene has been replaced
110 with GFP (VSVΔG-GFP). Next, the infectivity of the resulting particles was assayed on VeroE6 cells
111 expressing the TMPRSS2 cofactor by counting GFP-positive cells. VSVΔG-GFP particles were
112 pseudotyped with the native SARS-CoV-2 Wuhan-Hu-1 S protein as a positive control and reference
113 value (WT). No infection was observed when the TMD of the SARS-CoV-2 S protein was eliminated
114 (ΔTMD) or was substituted by a scrambled version of the TMD (SCRBL) where the composition of
115 the residues included in the TMD was preserved but their position was randomly varied, confirming
116 the importance of the SARS-CoV-2 S protein TMD in the entry process and indicating a role beyond
117 membrane anchoring (Fig 2B). Expression of the chimeras included in this work can be found in
118 Supp Fig 1.

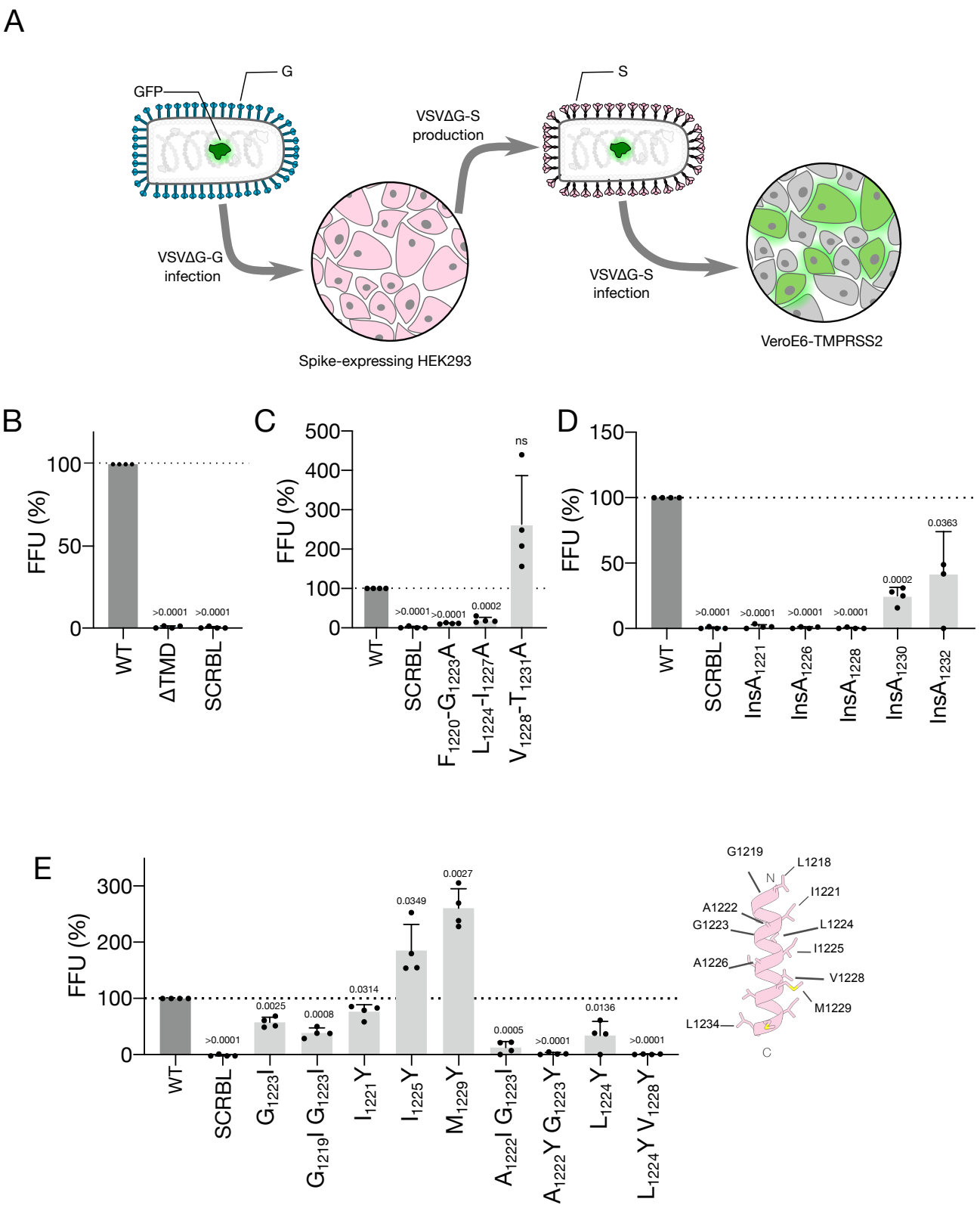

Figure 2. VSVΔG-GFP pseudotyped virus assay. **A**. Generation of VSVΔG-GFP pseudotyped particles. HEK293T cells were transfected with the corresponding SARS-CoV-2 S protein variant and infected with a VSV lacking the G gene and expressing GFP (VSVΔG-GFP). The resulting virus, incorporating the S variants on its surface (VSVΔG-GFP -S), was

recovered from the media and used to infect Vero-TMPRSS2 cells. Viral infectivity was then analyzed by counting GFP-positive cells. **B-E**. Focus Forming Units (FFU) measured after infection with VSVΔG-GFP pseudotyped with different variants of the SARS-CoV-2 S protein TMD. All samples were normalized to the wild-type SARS-CoV-2 S protein (WT). The p-values (<0.05) for individual one-sample t-tests (vs WT) are indicated above each bar. **B**. FFU from VSVΔG-GFP particles decorated with the wild-type SARS-CoV-2 S protein (WT), the SARS-CoV-2 S protein where TMD was eliminated (ΔTMD), and a scrambled version of the SARS-CoV-2 S protein TMD (SCRBL). **C**. FFU from pseudotyped VSVΔG-GFP with the SARS-CoV-2 S protein with substitutions of amino acid stretches, Phe_{1220} to Gly_{1223}, Leu_{1224} to Ile_{1227}, and Val_{1228} to Thr_{1231}, with alanine (Phe_{1220}-Gly_{1223}A, Leu_{1224}-Ile_{1227}A, and Val_{1228}-Thr_{1231}A respectively). **D**. FFU from pseudotyped VSVΔG-GFP with the SARS-CoV-2 S protein including alanine insertions at positions 1221, 1226, 1228, 1230, and 1232 ($InsA_{1221}$, $InsA_{1226}$, $InsA_{1228}$, $InsA_{1230}$, and $InsA_{1232}$). **E**. FFU from pseudotyped VSVΔG-GFP with the SARS-CoV-2 S protein bearing the following point mutations Gly_{1223} to Ile, Gly_{1219} to Ile and Gly_{1223} to Ile, Ile_{1221} to Tyr, Ile_{1225} to Tyr, Met_{1229} to Tyr, Ala_{1222} to Ile and Gly_{1223} to Ile, Ala_{1222} to Tyr, and Gly_{1223} to Tyr, Leu_{1224} to Tyr, Leu_{1224} to Tyr, and Val_{1228} to Tyr (G_{1223}I, G_{1219}I G_{1223}I, I_{1221}Y, I_{1225}Y, M_{1229}Y, A_{1222}I G_{1223}I, A_{1222}Y G_{1223}Y, L_{1224}Y, L_{1224}Y V_{1228}Y, respectively).

Next, stretches of four amino acids (one helical turn) on the SARS-CoV-2 S protein TMD, starting at Phe_{1220}, were substituted with alanine residues (Fig 2C). Substitution of the section covering Phe_{1220}-Gly_{1223} and Leu_{1224}-Ile_{1227} (F_{1220}-G_{1223}A and L_{1224}-I_{1227}A respectively) greatly diminishes the infectivity of the pseudo-typed VSVΔG-GFP particles. Substitution of Val_{1228}-Thr_{1231} (V_{1228}-T_{1231}A) to alanines did not decrease viral entry, on the contrary, a non-significant increase was observed. These results indicate that the sequence and structural parameters of the TMD relevant for viral entry are distributed across the entire segment, with a stronger implication of the N-terminal portion of the TMD. It is important to note that none of the modifications included in the study significantly modified the insertion potential of the SARS-CoV-2 S protein TMD based on the predicted ΔG_{app} for their insertion (Fig 1B).

149 To further analyze the role of SARS-CoV-2 S protein TMD in the viral entry process we inserted
150 alanine residues in key positions of the hydrophobic segment (Fig 2D). Inserting a residue not only
151 increases the length of the TMD but also changes the relative orientation of the residues positioned
152 before and after the insertion point due to the α-helical nature of this segment[27]. We first inserted an
153 alanine between Phe_{1220} and Ile_{1221} (Ins-A_{1221}) which alters the relative orientation of the aromatic
154 membrane proximal region and the TMD. Additionally, Ins-Ala_{1221} disrupts the $G_{1223}xxxG_{1229}$ motif
155 found in the TMD[14], forcing a 100º rotation for Gly_{1219} relative to Gly_{1223} (Supp Fig 2A vs 2B). As
156 shown in Fig 2D, Ins-Ala_{1221} greatly reduced the infectivity of pseudo-typed VSVΔG-GFP particles
157 suggesting that either the relative orientation of the aromatic stretch vs the TMD, the GxxxG
158 interaction motif, or both are important for particle entry.
159
160 Insertion of an alanine residue in positions 1226 or 1228 (Ins-A_{1226} and Ins-A_{1228}) negatively affected
161 viral entry, indicating that the relative orientation of the N-terminal and C-terminal sections of the
162 TMD might be important for infectivity (Fig 2D). These two insertion points were selected with the
163 work of Fu and Chou[16] in mind, who proposed a trimerization hydrophobic zipper involving residues
164 1221, 1225, 1229, and 1233. Thus, the observed reduction in viral entry could also result from
165 disrupting the oligomerization motif they described.
166
167 Insertions at positions 1230 and 1232 (Ins-A_{1230} and Ins-A_{1232}) also disturb the hydrophobic
168 trimerization motif proposed by Fu and Chou (Supp Fig. 2), but reduced particle entry to a lesser
169 extent than Ins-A_{1226} or Ins-A_{1228} (Fig 2D). Of these two insertions, Ins-A_{1230} reduced pseudo-typed
170 VSVΔG-GFP entry more than Ins-A_{1232}, suggesting that the relative orientation of the N-terminal and
171 C-terminal sections of the TMD is more important for the protein function than the trimerization
172 hydrophobic zipper. Note that while the authors[16] included leucine residues on positions 1229 and

173 1233 we incorporated the methionine residues found in the SARS-CoV-2 S protein consensus
174 sequence (Uniprot: P0DTC2).
175
176 To further analyze the impact of the GxxxG and the hydrophobic zipper as oligomerization motifs,
177 we selectively mutated key residues in the SARS-CoV-2 S protein. First, we replaced Gly_{1223} with
178 isoleucine ($G_{1223}I$) since the equivalent substitution is sufficient to break the dimerization of
179 Glycophorin A (GpA) TMD[28,29]. The GFP count associated with pseudo-typed VSVΔG-GFP entry
180 revealed that the $G_{1223}I$ mutation is sufficient to reduce viral entry (Fig 2E). Substituting Gly_{1219} and
181 Gly_{1223} with isoleucine ($G_{1219}I$ $G_{1223}I$) further decreases pseudo-typed VSVΔG-GFP infectivity. Next,
182 we replaced Ile_{1221}, Ile_{1225}, or Met_{1229} with tyrosine ($I_{1221}Y$, $I_{1225}Y$, and $M_{1229}Y$), changes that were
183 previously suggested to modify TMD homo-oligomerization[16]. While the $I_{1221}Y$ substitution slightly
184 reduced viral entry, the $I_{1225}Y$, and $M_{1229}Y$ ones did not (Fig 2E).
185
186 A closer look at the SARS-CoV-2 TMD reveals a highly hydrophobic surface composed of Leu_{1218},
187 Ile_{1221}, Leu_{1224}, Ile_{1225}, Val_{1228}, and Ile_{1232} and an opposing surface rich in small residues including
188 Gly_{1219}, Ala_{1222}, Gly_{1223}, and Ala_{1226} which could participate in TMD-TMD interactions[15,28–31] (Fig
189 1C). To analyze the importance of these regions, we first replaced Ala_{1222} and Gly_{1223} with isoleucine
190 ($A_{1222}I$ $G_{1223}I$) and measured the impact on the pseudo-typed VSVΔG-GFP infectivity. Our results
191 revealed that the $A_{1222}I$ $G_{1223}I$ mutant is less able to promote viral entry than the previously tested
192 $G_{1223}I$ mutant (Fig 2E). When Ala_{1222} and Gly_{1223} were replaced with tyrosine ($A_{1222}Y$ $G_{1223}Y$), a
193 larger and less hydrophobic amino acid, we observed a greater reduction in VSVΔG-GFP infectivity.
194 Similarly, substituting Leu_{1224} with tyrosine ($L_{1224}Y$) on the hydrophobic surface also reduced
195 VSVΔG-GFP entry. Double substitution of Leu_{1224} and Val_{1228} to tyrosine ($L_{1224}Y$ $V_{1228}Y$) diminished
196 VSVΔG-GFP infectivity further. According to our results, both the small residues and the

197 hydrophobic bulky residues aligned on opposing faces of the helix (Fig 2E) are relevant for the entry
198 process, probably because they participate in protein-protein interactions or in TMD-lipid
199 interactions. Protein levels for all the chimeras were probed by western blotting to avoid
200 misinterpretation of the data (Supp. Fig 1).
201
202 To incorporate the SARS-CoV-2 S protein into VSVΔG-GFP pseudo-particles it must be located at
203 the plasma membrane. Thus, we investigated whether those events in which no VSVΔG-GFP pseudo-
204 particle infectivity was observed were the consequence of SARS-CoV-2 S protein absence at the cell
205 surface. We determined whether the SARS-CoV-2 S protein was located at the plasma membrane by
206 surface-staining with an anti-RBD antibody followed by flow cytometry analysis (**Fig 3**). All SARS-
207 CoV-2 S protein variants that showed a decreased VSVΔG-GFP infectivity were included in this
208 assay. Additionally, the WT S protein was used as a positive control while the ΔTMD variant was
209 included as a negative control (**Fig 3A**). Our results indicate that all SARS-CoV-2 S protein variants
210 were present at the plasma membrane at similar levels except for Ins-A_{1228} (**Fig 3B and Supp. Fig**
211 **3A**). Thus validating the results of the VSVΔG-GFP pseudo-particle assay. The absence of Ins-A_{1228}
212 at the cell surface suggests that the SARS-CoV-2 S protein TMD might play a role in protein
213 trafficking.
214

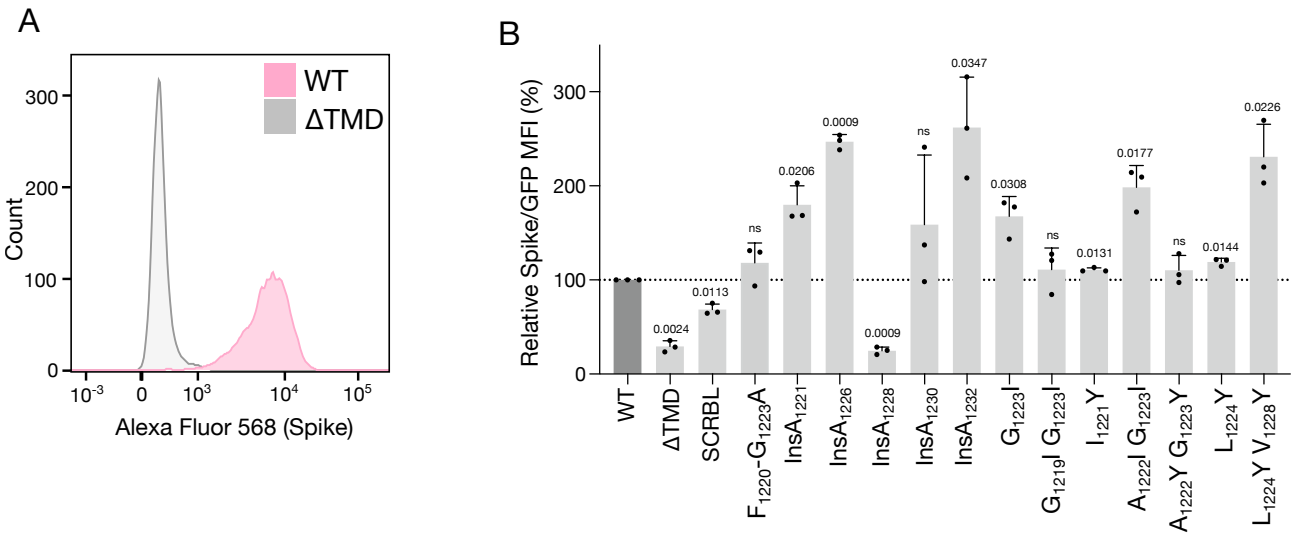

Figure 3. Surface expression of Spike variants. **A.** Spike surface expression of WT and ΔTMD controls analyzed by flow cytometry. HEK293T cells were transfected with plasmids encoding the corresponding S protein alongside a constitutively GFP-expressing plasmid. After 48 hours, cells were stained with an anti-RBD antibody. Levels of the surface SARS-CoV-2 S protein (red) and GFP (green) were analyzed by flow cytometry. **B.** Relative surface expression of all Spike variants tested in this assay. GFP was used as a transfection control. The figure shows the mean fluorescence intensity (MFI) of SARS-CoV-2 S protein vs GFP signal ratio. Samples were normalized to the SARS-CoV-2 S protein WT. The significative p-values (<0.05) for individual one-sample t-tests vs. WT are indicated above each bar.

BiMuC assay for the analysis of membrane fusion

The role of the SARS-CoV-2 S protein TMD during the viral and cellular membrane fusion process was corroborated with a syncytia-based assay known as BiMuC[30,31]. Briefly, the Venus Fluorescent Protein (VFP) can be split into two fragments, VN and VC, neither of which is fluorescent. However, when these two fragments are fused to a pair of interacting proteins that bring them together, such as cJun and bFos, the structure of the VFP is reconstituted and the fluorescence is recovered. The VN-cJun and VC-bFos chimeras were expressed in separated cell pools together with the viral machinery required for membrane fusion. Therefore, the two chimeras would only meet in the event of membrane fusion (**Fig 4A**). The complete SARS-CoV-2 S WT protein was used as a positive control

233 and reference value. The ΔTMD and SCRBL variants were included as negative controls (**Fig 4B**).

234 Measurements of the area of the syncytia can be found in Supp. Fig 3.

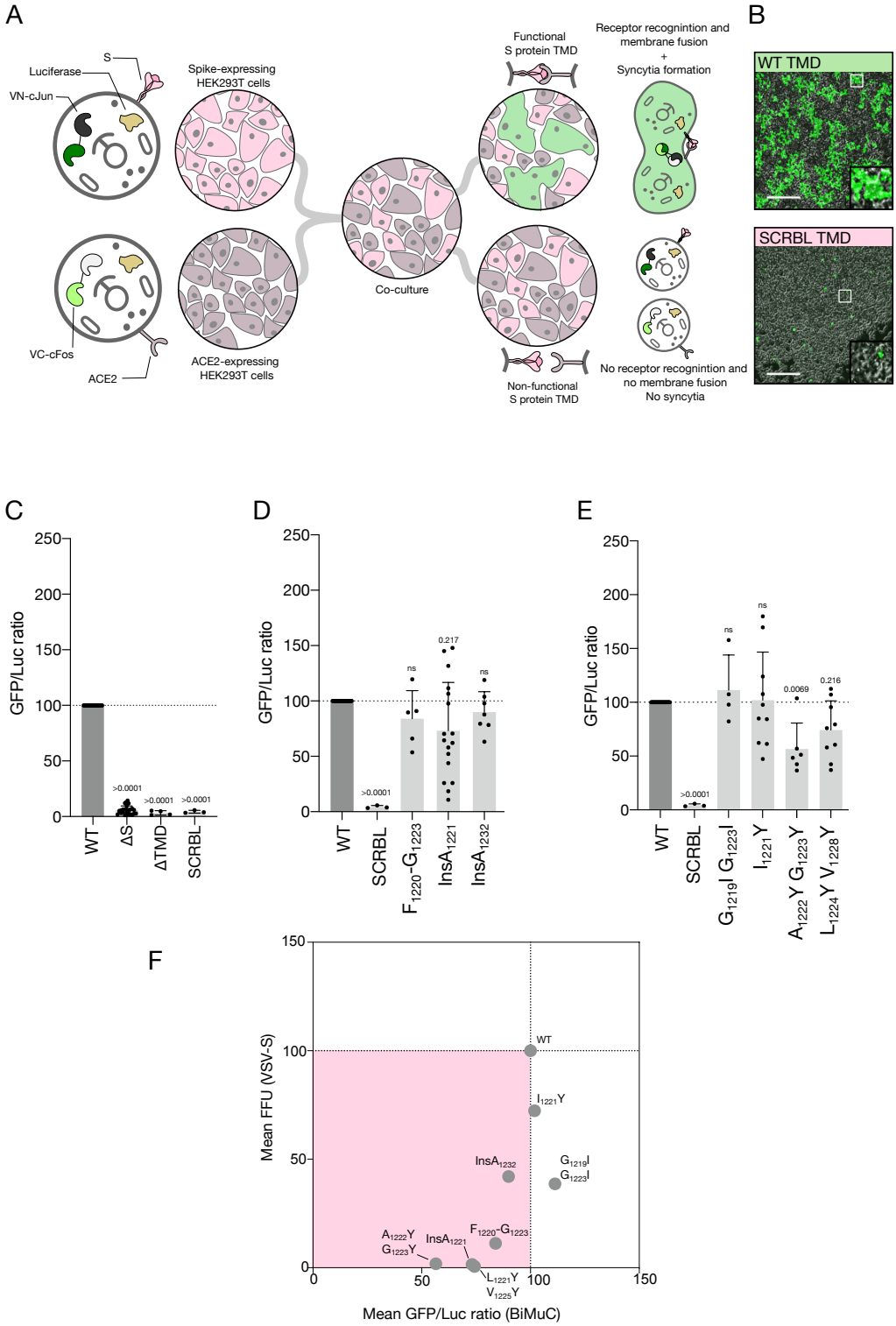

235

236 ***Figure 4. Analysis of SARS-CoV-2 S protein membrane fusion properties by BiMuC***. **A**. Schematic representation of

237 the BiMuC assay. The Venus fluorescence protein (VFP) can be split into two fragments, VN and VC respectively, neither

238 of which is fluorescent. These two fragments were fused to cJun and bFos (VN-cJun and VC-bFos) and transfected into
239 HEK 293T cells in separated cell pools. Cells were co-transfected with the viral machinery required for membrane fusion,
240 the corresponding SARS-CoV-2 S protein, and the ACE2 receptor. Additionally, both cell pools were transfected with the
241 Renilla Luciferase (luciferase) to normalize the fluorescent values. Only functional SARS-CoV-2 S proteins facilitated
242 the S - ACE2 recognition and membrane fusion allowing VFP reconstitution and fluorescence. **B.** Representative images
243 of the assay where cells have been transfected with the SARS-CoV-2 S protein (WT) or the SARS-CoV-2 S protein
244 bearing a scrambled version of the TMD (SCRBL). **C-E**. Fluorescence/luciferase signal ratio (GFP/Luc ratio) was
245 measured for the SARS-CoV-2 S protein variants tested on this assay. Samples were normalized to the SARS-CoV-2 S
246 protein WT. Significative p-values (<0.05) for individual one-sample t-tests are indicated above each bar. **C**. GFP/Luc
247 ratio for the SARS-CoV-2 S protein (WT), the SARS-CoV-2 S protein where TMD was eliminated (ΔTMD), and a
248 chimera bearing a scrambled version of the SARS-CoV-2 S protein TMD (SCRBL). As a negative control we also
249 included cells that did not incorporate the SARS-CoV-2 S protein (ΔS). **D**. GFP/Luc ratio for the SARS-CoV-2 S protein
250 with substitutions of 4 amino acid stretches Phe_{1220} to Gly_{1223}, and Val_{1228} to Thr_{1231}, by alanines (Phe_{1220}-Gly_{1223}A and
251 Val_{1228}-Thr_{1231}A), and the SARS-CoV-2 S protein including alanine insertions in positions 1221, 1228, and 1232 ($InsA_{1221}$,
252 $InsA_{1228}$, and $InsA_{1232}$). **E**. GFP/Luc ratio for the SARS-CoV-2 S protein bearing the following point mutations: Gly_{1219}
253 to Ile and Gly_{1223} to Ile, Ile_{1221} to Tyr, Ile_{1225} to Tyr, Met_{1229} to Tyr, Ala_{1222} to Tyr and Gly_{1223} to Tyr, and Leu_{1224} to Tyr and
254 Val_{1228} to Tyr ($G_{1219}I$ $G_{1223}I$, $I_{1221}Y$, $I_{1225}Y$, $M_{1229}Y$, $A_{1222}Y$ $G_{1223}Y$, and $L_{1224}Y$ $V_{1228}Y$, respectively). All panels include the
255 WT values used to normalize the data (dotted line) and the SCRBL samples. **F**. Correlation of FFU measured in the
256 VSVΔG-GFP infection assay against values of reconstituted GFP/Luc ratio in the BiMuC fusion assay. Colors show
257 samples that have lower signals than WT values in both systems (pink background), higher in both systems (green
258 background) or different between the two assays (white background).
259

260 Next, we selected some of the previously described variants of the S protein and tested them using
261 the BiMuC methodology. Substituting the Phe_{1220}-Gly_{1223} helical turn with alanines (F_{1220}-G_{1223}A)
262 diminished syncytia formation, though not significantly (**Fig 4D**). On the other hand, V_{1228}-T_{1231}A
263 did not reduce syncytia formation (**Fig 4D**). Alanine insertions Ins-A_{1221} altered the observed
264 syncytia-derived fluorescence (**Fig 4D**). However, only a small non-significant reduction in syncytia
265 formation was observed for Ins-A_{1232}. We also tested the influence of point mutations on the ability

266 of the SARS-CoV-2 S protein to induce syncytia formation (**Fig 4E**). In this case, the $G_{1219}I$ $G_{1223}I$,
267 $I_{1221}Y$, or the $M_{1229}Y$ substitutions did not perturb the SARS-CoV-2 S protein function. However,
268 $I_{1225}Y$, $A_{1222}Y$ $G_{1223}Y$, and $L_{1224}Y$ $V_{1228}Y$ reduced the formation of syncytia. Altogether, the BiMuC-
269 derived results correlate with the pseudo-typed VSVΔG-GFP assay (**Fig 4F)**.
270

271 **Analysis of TMD oligomerization**

272 Some of the modifications included in the BiMuC and the pseudo-typed VSVΔG-GFP assay could
273 alter the previously described homo-oligomerization of the SARS-CoV-2 TMD[12,16,32]. To directly
274 analyze the SARS-CoV-2 TMD potential oligomer, we used a bimolecular fluorescent
275 complementation (BiFC) approach adapted to study intramembrane interactions[33–36]. Briefly, the
276 tested TMDs were fused to a split VFP, either to its N-terminal (VN) or its C-terminal (VC). If
277 interaction between the tested TMDs occurs, it will bring the VN and VC ends together, facilitating
278 the reconstitution of the VFP structure and causing fluorescence **(Fig 5A**). The TMD of GpA was
279 used as a positive control and normalization value across experimental replicates. The TMD of
280 Tomm20, a monomeric hydrophobic segment, was used as a negative control[35,37].

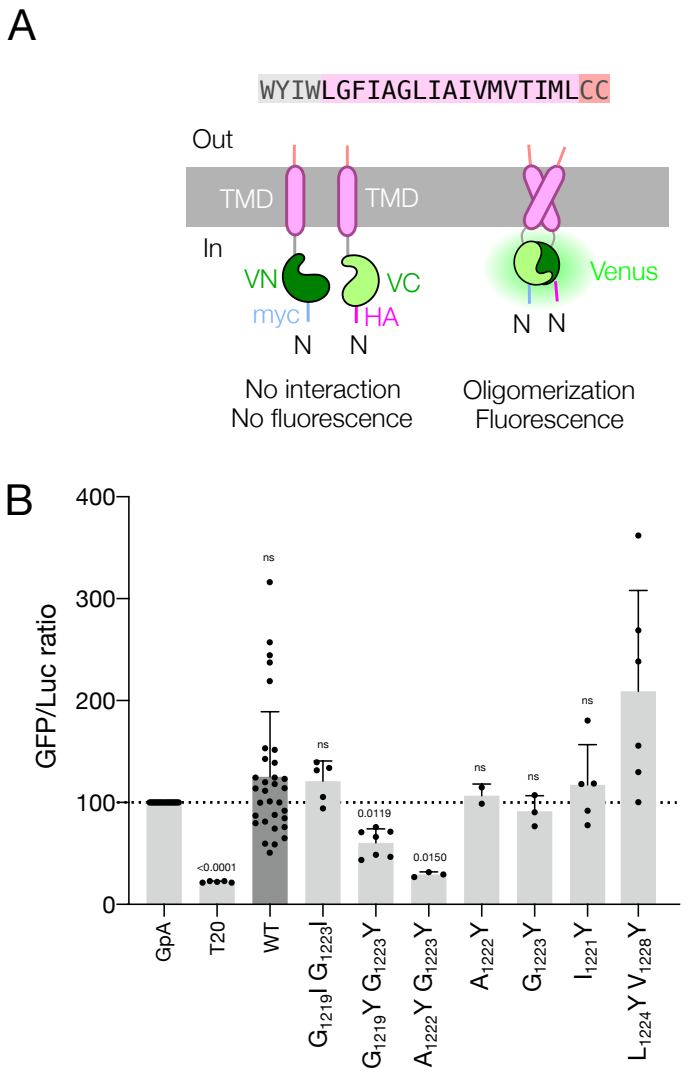

281

282 ***Figure 5. Analysis of TMD oligomerization by BiFC assay***. **A**. Reconstitution of the Venus Fluorescent Protein (VFP)
283 mediated by the SARS-CoV-2 S protein TMD oligomerization. Different S TMD mutants were fused to both the N and
284 C terminal sections of the VFP (VN and VC, respectively) and expressed in HEK 293T cells together with the Renilla
285 Luciferase. If the SARS-CoV-2 S protein TMD can to oligomerize the VFP will be reconstituted **B.** GFP/Luc ratios
286 measured for different chimeras bearing the, Glycophorin A TMD (GpA), *E.coli* Lep H2, wild-type SARS-CoV-2 S
287 protein TMD (WT), and the SARS-CoV-2 S protein TMD with the following point mutations $G_{1219}I$ Gly_{1223} to Ile, Gly_{1219}
288 to Tyr and Gly_{1223} to Tyr, Ala_{1222} to Tyr and Gly_{1223} to Tyr, Ala_{1222} to Tyr, Gly_{1223} to Ile, Ile_{1221} to Tyr, Ile_{1225} to Tyr, Met_{1229}
289 to Tyr, and Leu_{1224} to Tyr and Val_{1228} to Tyr ($G_{1219}I$ $G_{1223}I$, $G_{1219}Y$ $G_{1223}Y$, $A_{1222}Y$ $G_{1223}Y$, $A_{1222}Y$, $G_{1223}I$, $I_{1221}Y$, $I_{1225}Y$,
290 $M_{1229}Y$ and $L_{1224}Y$ $V_{1228}Y$ respectively). All values are normalized against GpA homo-oligomer. The significative p-values
291 (<0.05) for individual one-sample t-tests are indicated above each bar.

292

293 Using this BiFC assay, we tested the SARS-CoV-2 TMD. Our results indicate that this TMD is
294 sufficient for inducing oligomerization (**Fig 5B**). Next, we focused on the role of the surface with
295 small residues on the oligomerization of the TMD. The $G_{1219}I$ $G_{1223}I$ substitution did not decrease the
296 SARS-CoV-2 S protein's TMD oligomerization potential, however, the $G_{1219}Y$ $G_{1223}Y$ did, a result
297 that correlates with the outcome of the BiMuC assay. The $A_{1222}Y$ $G_{1223}Y$ double substitution further
298 reduced oligomerization. Interestingly, the substitution of only Ala_{1222} or Gly_{1223} with Y ($A_{1222}Y$ and
299 $G_{1223}Y$), did not alter the oligomerization capabilities of the SARS-CoV-2 TMD, suggesting a
300 synergistic effect of these two residues.
301
302 We also tested the role of the bulky hydrophobic helix interface on the SARS-CoV-2 S protein TMD
303 on oligomerization. The single substitutions $I_{1221}Y$, $I_{1225}Y$, or $M_{1229}Y$ did not alter oligomerization.
304 Furthermore, the double substitution $L_{1224}Y$ $V_{1228}Y$, which had proven fundamental for VSVΔG-GFP
305 entry and membrane fusion in the BiMuC assay, did not decrease the observed fluorescence,
306 suggesting that the hydrophobic surface does not participate in the oligomerization of the SARS-
307 CoV-2 S protein TMD.
308
309 We modeled the potential SARS-CoV-2 S protein TMD homo-trimer using TMHOP[38]. TMHOP uses
310 Rosetta symmetric all-atom ab initio fold-and-dock simulations in an implicit membrane environment
311 to predict low-energy conformations based on the empirical measurement of amino acid insertion
312 propensities into *E. coli* inner membrane[39]. These conformations are clustered based on energy and
313 structural properties (Supp Fig. 4A) and a representative model of each cluster is shown (**Fig 6A**). In
314 each model, Gly_{1216}, Ala_{1222}, Gly_{1223}, and Ala_{1226} are located on the interaction surface of the potential
315 trimer, confirming our experimental results. We also modeled the potential TMD trimer using
316 AlphaFold3[40], a recent evolution of the AlphaFold2 architecture and training procedure capable of
317 predicting the joint structure of complexes. Once again, the predicted models present, in most cases,

318 Gly_{1216}, Ala_{1222}, Gly_{1223}, and Ala_{1226} at the interior of a TMD homo-trimer (**Fig. 6B** and Supp Fig. 4).
319 The AlphaFold3 server allowed us to model larger sequences, including the full-length S protein.
320 When the TMD region was modeled in the context of the full-length protein accuracy was low and
321 thus the models were discarded (**Supp. Fig 5**). However, the server modeled with sufficient
322 confidence the TMD flanked by the N-terminal aromatic-rich region and the Cys-rich C-terminal end.
323 The retrieved models for this section included, once again, the Gly_{1216}, Ala_{1222}, Gly_{1223}, and Ala_{1226}
324 on the internal surface of a TMD trimer (**Fig. 6C** and Supp Fig. 4).

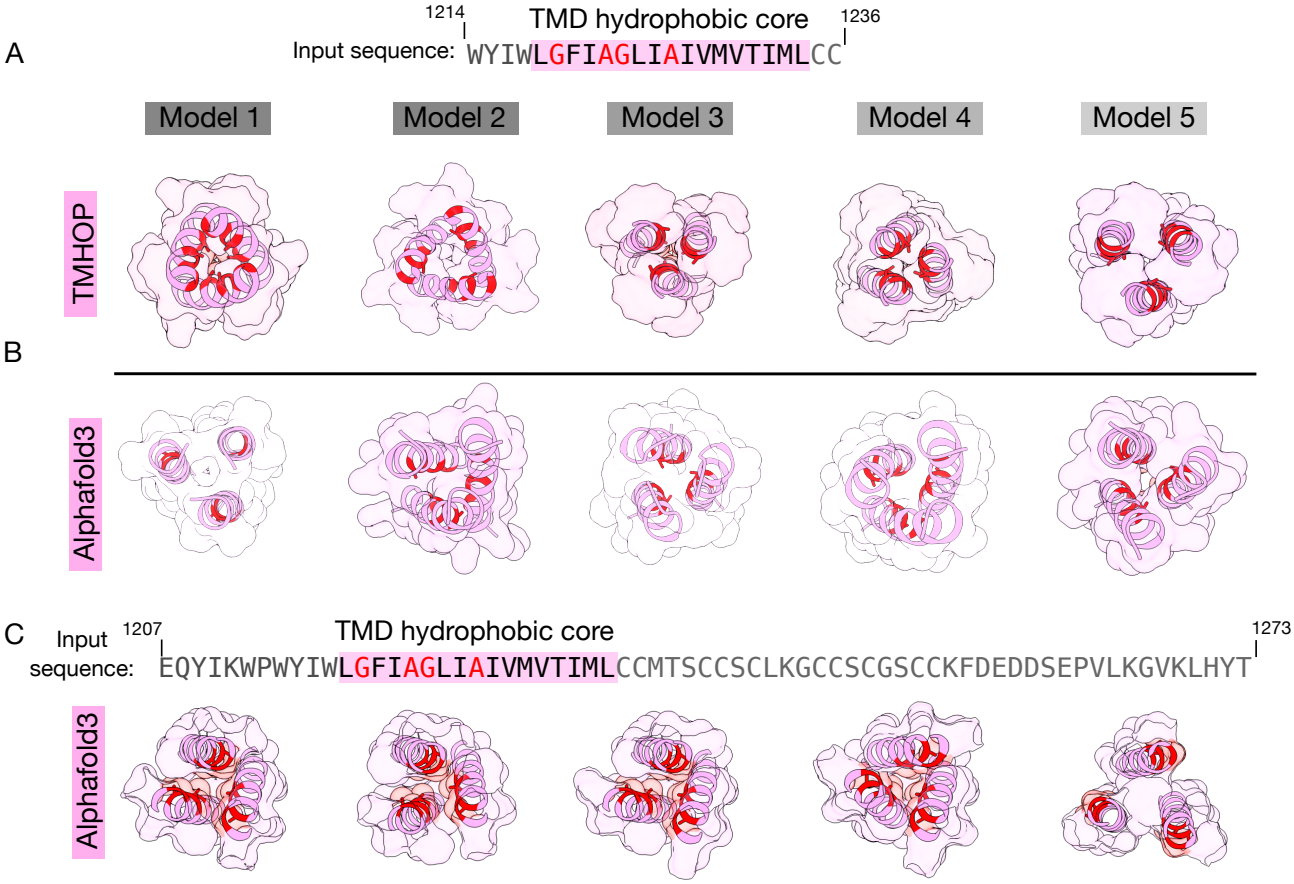

325

326 ***Figure 6. SARS-CoV-2 S protein TMD* trimer models. A and B.** SARS-CoV-2 S protein TMD trimer modeled by the
327 TMHOP server (**A**) and by the AlphaFold3 server (**B**). The top five models are shown. The input sequence was
328 $_{1212}$WYIWLGFIAGLIAIVMVTIMLCC$_{1235}$. Models show the TMD hydrophobic core, residues 1218-1234 shown in
329 pink. The secondary structure as well as the surface of the peptide is shown. Gly_{1216}, Ala_{1222}, Gly_{1223}, and Ala_{1226} are
330 highlighted in red on the secondary structure representation. **C**. AlphaFold3 server model of the C-terminal region of the
331 SARS-CoV-2 S protein, including the aromatic-rich section, the TMD, and the cysteine-rich domain. The five top models

are shown. Models include just the TMD hydrophobic core, residues 1218-1234 shown in pink. The secondary structure as well as the surface of the TMD hydrophobic core is shown. Gly_{1216}, Ala_{1222}, Gly_{1223}, and Ala_{1226} are highlighted in red.

Discussion

In sum, our results indicate that the SARS-CoV-2 S protein TMD is a key region for viral entry. A variety of small changes across its sequence can render a crippled S protein. One could imagine that a passive membrane anchoring domain would accept mutations as long as the overall hydrophobicity and length are not compromised. However, a closer look at the genome of all the variants of SARS-CoV-2 reveals that no mutation whatsoever has been found in the S protein TMD, and few variations are found between SARS-CoV-2, the SARS-CoV-1, or MERS-CoV (Supp Fig 5A), while TMDs of other SARS-CoV-2 proteins present multiple mutations (Supp Fig 5B).

Within the S protein TMD, we identified at least two subdomains important for the protein's function. One is a highly hydrophobic surface that most likely works in coordination with the lipid milieu, and the other is a surface rich in small residues (alanine and glycine) which might participate in the homo-oligomerization of the TMD. In the non-polar membrane environment, the hydrophobic effect is responsible for insertion into the membrane and does not usually contribute to the tertiary and quaternary structure[41]. Furthermore, the nature of the residues that facilitate membrane insertion impedes salt bridges and hydrogen bonds between TMDs[42]. In this context, the tertiary and quaternary structure of TMDs is dictated by a delicate balance of the remaining low energy forces, where van der Waals interactions play a crucial role[43]. The nature of van der Waals forces requires a large contact area between the associating protein segments. Amino acids with small side chains such as glycine and alanine facilitate the helix-helix contact increasing van der Waals forces. In this scenario, the inclusion of bulky residues that diminish the helix-helix contact area could break TMD-TMD interactions. Our results, together with the structural and sequence analysis, suggest that the SARS-

357 CoV-2 S protein TMD is capable of forming homo-trimers held together by van der Waals forces.
358 However, the structure of the full-length S protein in a post-fusion conformation did not reveal the
359 TMD in a trimeric disposition[17]. In this structure, the TMDs surround the FPs and make contact with
360 them through the Leu_{1234} and Phe_{1120} residues, which were not involved in either of the subdomains
361 described in our work. Nonetheless, given that different oligomeric states coexist for the SARS-CoV-
362 2 S protein[44], it is conceivable that the TMDs could be found in different oligomerization states as
363 well. Furthermore, recent simulations suggest that the SARS-CoV-2 spike TMD is inherently
364 dynamic with different possible conformations, monomer, dimer and trimer[32]. This conformation
365 variety may be required for viral fusion. In the early stages of the SARS-CoV-2 S protein biogenesis,
366 the TMD-TMD interactions responsible for the TMD trimer could facilitate the formation of a full-
367 length protein trimer together with other motifs[8], participate in the post-translational processing of
368 the S protein[45], or modulate its trafficking[46]. Next, the low energy nature of the forces holding the
369 TMD trimer together would allow the transition between the different oligomeric states of the protein
370 required during the complex membrane fusion process.
371
372 Our work goes beyond understanding viral entry. Recently, TMDs and their interactions have been
373 targeted for the modulation of protein function and the development of new therapeutic
374 approaches[37,47]. Our results are the first step in the development of a potential new strategy for the
375 inhibition of SARS-CoV-2 infection.
376

377 ## Materials and Methods

378 **Plasmid constructs**

379 Sequence encoding SARS-CoV-2 S protein (Addgene #164433) was a gift from Alejandro Balazs.
380 All subsequent mutants were obtained with the Pfu Plus! mutagenesis kit (EurX, Gdańsk, Poland)
381 according to the manufacturer's instructions. For the generation of BiFC chimeric plasmids, the

382 sequence encoding for the TMD was PCR amplified and subcloned to generate a fusion with the Nt
383 or Ct of the Venus Fluorescent Protein (VN, VC, respectively: Addgene #27097 and #22011, a gift
384 from Chang-Deng H). The TMD was cloned at the Ct of the VFP. These constructs were generated
385 using In-Fusion HD cloning kit (Takara, Japan) also according to the manufacturer's instructions.
386 Sequences were verified by sequencing the plasmid DNA at Macrogen (Seoul, South Korea).
387
388 **Human cells and culture conditions**
389 Human embryonic kidney (HEK293T) (from American Type Cell Collection, Manassas, VA, USA)
390 were maintained in Dulbecco's modified Eagle's medium (DMEM, Gibco) supplemented with 10 %
391 fetal bovine serum, 1 % penicillin-streptomycin (Sigma Aldrich, St. Louis, MO, USA), and 1 % MEM
392 non-essential amino acids. Cells were maintained at 37°C and 5 % CO_2 conditions. VeroE6-
393 TMPRSS2 were obtained from the JCRB Cell Bank (catalog JCRB1819). Cells were cultured in
394 DMEM with either 10% or 2% FBS for maintenance or infection, respectively. Selection of VeroE6-
395 TMPRSS2 was performed using media containing 1 mg/mL G418 (Cat. no. A1720, Sigma).
396
397 **Transient DNA transfections**
398 HEK 293T were seeded in 6, 12 or 24-well plates and grown in DMEM (Gibco) supplemented with
399 10 % fetal bovine serum (FBS, Gibco) the day before transfection. For the pseudo-typed VSVΔG-
400 GFP assay, transfections were carried out with calcium phosphate. Briefly, DNA was mixed with
401 $CaCl_2$ 125 mM in HBS buffer (NaCl 140 mM, KCl 5 mM, Na_2HPO_4 750 µM, dextrose 6 mM, HEPES
402 25 mM pH 7.05), incubated for 15 minutes and added to the HEK293 cells. For the rest of
403 transfections, DMEM medium was mixed with plasmid DNA (up to a total of 4 µg DNA for 6-well,
404 2 µg for 12-well plates) and transfected into HEK293T cells adding 3 µl of PEI 1 mg/ml and 100 µl
405 of DMEM per µg of DNA. For the surface expression analysis, 2-3 x 10^6 HEK293T cells were
406 transfected in 6 well-plates with the corresponding 1 µg Spike plasmid and 1 µg of a GFP encoding

407 plasmid. In the BiMuC assay, 2×10^6 HEK 293T cells in 6-well plates were transfected either with 1
408 μg of S and 1 μg of VN-Jun or with 1 μg ACE2 and 1 μg VC-Fos, plus 100 ng pRL-CMV.
409 Transfection mixtures were added dropwise onto cells and the media was changed after 24 hours. For
410 BiFC chimeras, 1 μg of cMyc-VN-TMD and 1 μg HA-VC-TMD were transfected into 2×10^6 HEK
411 293T cells in 12-well plates. A plasmid expressing Renilla luciferase under the CMV promoter (pRL-
412 CMV) (50 ng) was also added to the mix to normalize the signal. For western blot (WB) analysis, 2
413 μg of Spike plasmid was transfected into 6-well plates containing 6×10^6 HEK 293T cells.

414 **Pseudo-typed VSVΔG-GFP assay**

415 Pseudo-typed VSVΔG-GFP were pro duced by transfection of HEK 293T cells with lipofectamine
416 2000 (ThermoFisher Scientific) with a plasmid encoding the indicated S genes as indicated above in
417 a 24-well plate using 750 ng DNA and 1.875 μL of lipofectamine per well. Following 24 hours, cells
418 were infected at a multiplicity of infection of three with VSV lacking the VSV-G protein and encoding
419 both GFP and firefly luciferase[25] that was previously pseudotyped with the VSV-G protein to yield
420 infectious particles. Following infection, a monoclonal antibody targeting VSV-G (a kind gift of
421 Rafael Sanjuan, University of Valencia, Spain) was added to neutralize any remaining VSV-G bearing
422 viruses, and infected cells were incubated for 18 hours. The supernatant was collected, clarified and
423 frozen at -80ºC. The viral titer (focus forming units [FFU] per mL) was obtained by serial dilution on
424 VeroE6-TMPRSS2 cells in 96 well plates and counting of GFP-expressing cells using a live cell
425 microscope following 24 hours (Incucyte SX5, Sartorius).

426

427 **Flow cytometry**

428 Two days post-transfection, cells were washed once with PBS and detached by pipetting in 500 μl of
429 FACS buffer (0.1% sodium azide, 0.5% BSA in PBS). Then, 200 μl of cells were collected by
430 centrifugation at 1500 rpm for 5 min at 4ºC and stained with anti-SARS-CoV-2 RBD antibody
431 (Invitrogen, PA5-114529). After centrifugation, cells were incubated with Goat anti-Rabbit IgG

432 (H+L) AlexaFluor 568 (ThermoFisher, A11011). Antibodies were diluted to 1:1000 in FACS buffer
433 and 100 µl per sample was used for resuspending cells, following a 30 min incubation on ice in both
434 cases. After three final washes with FACS buffer, surface SARS-CoV-2 spike levels were analysed
435 using a LSRFortessa flow cytometer (BD Biosciences). Typically, 10,000 live cells were selected
436 based on morphology and acquired. SARS-CoV-2 spike levels were assessed by gating AlexaFluor
437 568 (excitation at 561 nm, collection at 586/15 nm) positive cells within the gate of GFP positive
438 cells (excitation at 488 nm, collection at 530/30 nm). Analysis was carried out using BDFACS Diva
439 8.0.2 and FlowJo X softwares.
440
441 **BiMuC assay**
442 One day post-transfection, media was discarded and cells rinsed with PBS. Then, 1 mL DMEM was
443 added to each well and one well expressing S and VN-Jun was pooled with other well expressing
444 hACE2 and VC-Fos. Cells were counted and each condition pool was divided into 4 wells of a 24-
445 well plate, each of those wells containing 3 x 10^5 cells. The next day, media was discarded in three of
446 the wells, cells rinsed with PBS, collected in 100 µl PBS, and seeded into 96-well black plates for
447 fluorescence read. Fluorescence was measured in a VictorX multi-plate reader (Perking Elmer,
448 Waltham, MA, USA). The luminescence was measured using the Renilla Luciferase Assay kit from
449 Sigma following the manufacturer protocol on 96-well white cell-culture plates. At least three
450 independent experiments were done. The ratio between VFP and luciferase was registered as the
451 relative fluorescence units (RFU) for each well. Each of those three wells was accounted as a technical
452 replicates, and the mean of the three values was taken as a biological replicate. RFU values were then
453 normalized against the wild-type condition. The extra well was used for imaging syncytia in a
454 fluorescence microscope.
455
456 **Fluorescence imaging**

457 For each condition, one well of a 24-well plate was used for imaging 24 h after co-culture of S and
458 hACE2 expressing cells. Images were acquired with a Zeiss Axiovert 5 fluorescence microscope both
459 with transmitted light and GFP channels with a 10X objective. Both images were overlayed and the
460 GFP area was quantified using Fiji[46].
461
462 **Bimolecular fluorescent complementation (BiFC) assay**
463 Two days after transfection, PBS washed and collected for fluorescence and luciferase measurements
464 (Victor X3 plate reader). For the Renilla luciferase readings used as signal normalization, we used
465 the Renilla Luciferase Glow Assay Kit (Pierce, Thermofisher) according to the manufacturer's
466 protocol. In each experiment, the fluorescence/luminescence ratio obtained with the GpA-GpA
467 homodimer was used for normalization. All experiments were done at least in triplicates.
468
469 **Protein expression and western blotting**
470 Two days after transfection, media was aspirated, cells rinsed with PBS and, lysed in 300 µl of
471 radioimmunoprecipitation assay (RIPA) buffer [150 mM NaCl, 50 mM tris-HCl (pH 8), 1% NP-40,
472 0.5 % sodium deoxycholate, 0.4% SDS, and 1 mM EDTA] supplemented with cOmplete EDTAfree
473 protease inhibitors (Roche). Lysates were sonicated with three pulses of 1 s in a VCX-500 Vibra Cell
474 sonicator (Sonics) following addition of 5X Laemmli´s sample buffer (final concentration 62.5 mM
475 Tris-HCl [pH 6.8], 2 % sodium dodecyl sulfate [SDS], 0.01 % bromophenol blue, 10 % glycerol and
476 5 % β-mercaptoethanol). Protein samples were boiled for 4 min at 95 ºC, subjected to 10 % SDS-
477 polyacrylamide gel electrophoresis (PAGE), and transferred to nitrocellulose membranes (Cytiva).
478 Membranes were blocked for 30 min at room temperature in Tris-buffered saline supplemented with
479 0.05 % Tween 20 (TBS-T) containing 5% non-fat dry milk and later incubated with primary
480 antibodies diluted in the same buffer at 4 °C overnight. Antibodies used in this study were SARS-
481 CoV-2 Spike S1 (Invitrogen PA5-81795), rabbit anti c-Myc (Sigma PLA0001) and mouse anti-

482 GAPDH (Santa Cruz sc-47724). Then, membranes were washed with TBS-T and incubated with goat
483 anti-rabbit or sheep anti-mouse IgG horseradish peroxidase conjugate (Sigma DC02L or GE
484 Healthcare NXA931, respectively) for 1 h at room temperature and washed again. All antibodies were
485 used at a 1:10,000 dilution in TBS-T with 5 % non-fat dry milk. Detection of immunoreactive proteins
486 was carried out using the enhanced chemiluminescence reaction (Amersham ECL Prime, Cytiva) and
487 detected by the Image Quant LAS 4000 Mini (GE Healthcare).

488 **Statistical analysis**

489 Unpaired t-tests assuming Gaussian distribution and equal standard deviation (SD) for all conditions
490 were applied. The p-value was two-tailed. One sample t-test was performed to compare different
491 wild-type-normalized conditions, comparing means with a 'hypothetical value' of 100. Significance
492 assessment between test samples and controls was performed using GraphPad Prism for P values <
493 0.05.

494

495 Acknowledgments

496 We thank P. Selvi and S. Pinto for their excellent technical assistance and V. Febrer for reviewing the
497 manuscript. This work was supported by the Generalitat Valenciana (CIPROM/2022/62) and grant
498 PID2020-119111GB-I00, PID2023-152568NB-I00 and CNS2022-135100 by
499 MCIN/AEI/10.13039/501100011033 and European Union NextGenerationEU/PRTR. J. O-M. has a
500 predoctoral contract granted by the Universisty of Valencia's "Atracció de Talent" programme (UV-
501 INV_PREDOC 1911519). D. B. had a research contract funded by CIPROM/2022/62 project. Flow
502 Cytometry experiments were carried out in the Cell Culture and Flow Cytometry facility at the SCSIE
503 (University of Valencia).

504 References

1. Yadav, R. *et al.* Role of Structural and Non-Structural Proteins and Therapeutic Targets of SARS-CoV-2 for COVID-19. *Cells* **10**, 821 (2021).
2. Gallagher, T. M. & Buchmeier, M. J. Coronavirus spike proteins in viral entry and pathogenesis. *Virology* **279**, 371–374 (2001).
3. Simmons, G., Zmora, P., Gierer, S., Heurich, A. & Pöhlmann, S. Proteolytic activation of the SARS-coronavirus spike protein: cutting enzymes at the cutting edge of antiviral research. *Antiviral Res.* **100**, 605–614 (2013).
4. Hoffmann, M. *et al.* SARS-CoV-2 Cell Entry Depends on ACE2 and TMPRSS2 and Is Blocked by a Clinically Proven Protease Inhibitor. *Cell* **181**, 271-280.e8 (2020).
5. Ellaithy, A., Gonzalez-Maeso, J., Logothetis, D. A. & Levitz, J. Structural and Biophysical Mechanisms of Class C G Protein-Coupled Receptor Function. *Trends Biochem. Sci.* **45**, 1049–1064 (2020).
6. Bocharov, E. V. *et al.* Helix-helix interactions in membrane domains of bitopic proteins: Specificity and role of lipid environment. *Biochim. Biophys. Acta Biomembr.* **1859**, 561–576 (2017).
7. Duart, G., Mingarro, I. & Martinez-Gil, L. The importance of transmembrane domain interactions in the viral control of apoptosis. *Mol. Cell. Oncol.* **8**, 1911290 (2021).
8. Barrett, C. T. & Dutch, R. E. Viral Membrane Fusion and the Transmembrane Domain. *Viruses* **12**, 693 (2020).
9. Mravic, M. *et al.* De novo-designed transmembrane proteins bind and regulate a cytokine receptor. *Nat. Chem. Biol.* **20**, 751–760 (2024).
10. Broer, R., Boson, B., Spaan, W., Cosset, F.-L. & Corver, J. Important role for the transmembrane domain of severe acute respiratory syndrome coronavirus spike protein during entry. *J. Virol.* **80**, 1302–1310 (2006).
11. Corver, J., Broer, R., van Kasteren, P. & Spaan, W. Mutagenesis of the transmembrane domain of the SARS coronavirus spike glycoprotein: refinement of the requirements for SARS coronavirus cell entry. *Virol. J.* **6**, 230 (2009).

12. Azad, T. *et al.* Implications for SARS-CoV-2 Vaccine Design: Fusion of Spike Glycoprotein Transmembrane Domain to Receptor-Binding Domain Induces Trimerization. *Membranes* **10**, 215 (2020).
13. Mackenzie, K. R. Folding and stability of alpha-helical integral membrane proteins. *Chem. Rev.* **106**, 1931–1977 (2006).
14. Arbely, E., Granot, Z., Kass, I., Orly, J. & Arkin, I. T. A trimerizing GxxxG motif is uniquely inserted in the severe acute respiratory syndrome (SARS) coronavirus spike protein transmembrane domain. *Biochemistry* **45**, 11349–11356 (2006).
15. Corver, J., Broer, R., van Kasteren, P. & Spaan, W. GxxxG motif of severe acute respiratory syndrome coronavirus spike glycoprotein transmembrane domain is not involved in trimerization and is not important for entry. *J. Virol.* **81**, 8352–8355 (2007).
16. Fu, Q. & Chou, J. J. A Trimeric Hydrophobic Zipper Mediates the Intramembrane Assembly of SARS-CoV-2 Spike. *J. Am. Chem. Soc.* **143**, 8543–8546 (2021).
17. Shi, W. *et al.* Cryo-EM structure of SARS-CoV-2 postfusion spike in membrane. *Nature* **619**, 403–409 (2023).
18. Hessa, T. *et al.* Molecular code for transmembrane-helix recognition by the Sec61 translocon. *Nature* **450**, 1026–1030 (2007).
19. Hessa, T. *et al.* Recognition of transmembrane helices by the endoplasmic reticulum translocon. *Nature* **433**, 377–381 (2005).
20. Sainz, B., Rausch, J. M., Gallaher, W. R., Garry, R. F. & Wimley, W. C. The aromatic domain of the coronavirus class I viral fusion protein induces membrane permeabilization: putative role during viral entry. *Biochemistry* **44**, 947–958 (2005).
21. Mesquita, F. S. *et al.* S-acylation controls SARS-CoV-2 membrane lipid organization and enhances infectivity. *Dev. Cell* **56**, 2790-2807.e8 (2021).
22. Wu, Z. *et al.* Palmitoylation of SARS-CoV-2 S protein is essential for viral infectivity. *Signal Transduct. Target. Ther.* **6**, 231 (2021).

23. McBride, C. E. & Machamer, C. E. Palmitoylation of SARS-CoV S protein is necessary for partitioning into detergent-resistant membranes and cell-cell fusion but not interaction with M protein. *Virology* **405**, 139–148 (2010).
24. Ujike, M. *et al.* Two palmitylated cysteine residues of the severe acute respiratory syndrome coronavirus spike (S) protein are critical for S incorporation into virus-like particles, but not for M-S co-localization. *J. Gen. Virol.* **93**, 823–828 (2012).
25. Bäuerl, C. *et al.* Assessment of SARS-CoV-2 neutralizing antibody titers in breastmilk from convalescent and vaccinated mothers. *iScience* **26**, (2023).
26. Berger Rentsch, M. & Zimmer, G. A vesicular stomatitis virus replicon-based bioassay for the rapid and sensitive determination of multi-species type I interferon. *PloS One* **6**, e25858 (2011).
27. Mingarro, I., Whitley, P., Lemmon, M. A. & von Heijne, G. Ala-insertion scanning mutagenesis of the glycophorin A transmembrane helix: a rapid way to map helix-helix interactions in integral membrane proteins. *Protein Sci. Publ. Protein Soc.* **5**, 1339–1341 (1996).
28. Lemmon, M. A., Flanagan, J. M., Treutlein, H. R., Zhang, J. & Engelman, D. M. Sequence specificity in the dimerization of transmembrane alpha-helices. *Biochemistry* **31**, 12719–12725 (1992).
29. Orzáez, M., Lukovic, D., Abad, C., Pérez-Payá, E. & Mingarro, I. Influence of hydrophobic matching on association of model transmembrane fragments containing a minimised glycophorin A dimerisation motif. *FEBS Lett.* **579**, 1633–1638 (2005).
30. García-Murria, M. J. *et al.* Identification of small molecules capable of enhancing viral membrane fusion. *Virol. J.* **20**, 99 (2023).
31. García-Murria, M. J., Expósito-Domínguez, N., Duart, G., Mingarro, I. & Martinez-Gil, L. A Bimolecular Multicellular Complementation System for the Detection of Syncytium Formation: A New Methodology for the Identification of Nipah Virus Entry Inhibitors. *Viruses* **11**, E229 (2019).
32. Lall, S., Balaram, P., Mathew, M. K. & Gosavi, S. Sequence of the SARS-CoV-2 Spike Transmembrane Domain Encodes Conformational Dynamics. *J. Phys. Chem. B* **129**, 194–209 (2025).

33. Kerppola, T. K. Design and implementation of bimolecular fluorescence complementation (BiFC) assays for the visualization of protein interactions in living cells. *Nat. Protoc.* **1**, 1278–1286 (2006).
34. Andreu-Fernández, V. *et al.* Bax transmembrane domain interacts with prosurvival Bcl-2 proteins in biological membranes. *Proc. Natl. Acad. Sci. U. S. A.* **114**, 310–315 (2017).
35. García-Murria, M. J. *et al.* Viral Bcl2s' transmembrane domain interact with host Bcl2 proteins to control cellular apoptosis. *Nat. Commun.* **11**, 6056 (2020).
36. Duart, G., Grau, B., Mingarro, I. & Martinez-Gil, L. Methodological approaches for the analysis of transmembrane domain interactions: A systematic review. *Biochim. Biophys. Acta Biomembr.* **1863**, 183712 (2021).
37. Duart, G. *et al.* Computational design of BclxL inhibitors that target transmembrane domain interactions. *Proc. Natl. Acad. Sci. U. S. A.* **120**, e2219648120 (2023).
38. Weinstein, J. Y., Elazar, A. & Fleishman, S. J. A lipophilicity-based energy function for membrane-protein modelling and design. *PLoS Comput. Biol.* **15**, e1007318 (2019).
39. Elazar, A. *et al.* Mutational scanning reveals the determinants of protein insertion and association energetics in the plasma membrane. *eLife* **5**, e12125 (2016).
40. Abramson, J. *et al.* Accurate structure prediction of biomolecular interactions with AlphaFold 3. *Nature* **630**, 493–500 (2024).
41. Martinez-Gil, L. & Mingarro, I. Viroporins, Examples of the Two-Stage Membrane Protein Folding Model. *Viruses* **7**, 3462–3482 (2015).
42. Baeza-Delgado, C., Marti-Renom, M. A. & Mingarro, I. Structure-based statistical analysis of transmembrane helices. *Eur. Biophys. J. EBJ* **42**, 199–207 (2013).
43. Toward understanding driving forces in membrane protein folding - ScienceDirect. https://www.sciencedirect.com/science/article/pii/S0003986114002823.
44. Webb, S. R., Smith, S. E., Fried, M. G. & Dutch, R. E. Transmembrane Domains of Highly Pathogenic Viral Fusion Proteins Exhibit Trimeric Association In Vitro. *mSphere* **3**, e00047-18 (2018).

45. Miyauchi, K. *et al.* The membrane-spanning domain of gp41 plays a critical role in intracellular trafficking of the HIV envelope protein. *Retrovirology* **7**, 95 (2010).
46. Popa, A. *et al.* Residues in the hendra virus fusion protein transmembrane domain are critical for endocytic recycling. *J. Virol.* **86**, 3014–3026 (2012).
47. Elazar, A. *et al.* De novo-designed transmembrane domains tune engineered receptor functions. *eLife* **11**, e75660 (2022).
48. Schindelin, J. *et al.* Fiji: an open-source platform for biological-image analysis. *Nat. Methods* **9**, 676–682 (2012).